Estimation of Strain Elastography from Ultrasound Radio-Frequency Data by Utilizing Analytic Gradient of the Similarity Metric

M. Omidyeganeh, *Member, IEEE*, Y. Xiao, *Member, IEEE*, M. O. Ahmad, *Fellow, IEEE*, and H. Rivaz,* *Member, IEEE*

***Abstract*— Most strain imaging techniques follow a pipeline strategy: in the first step, tissue displacement is estimated from radio-frequency (RF) frames, and in the second step, a spatial derivative operation is applied. There are two main issues that arise from this framework. First, the gradient operation amplifies noise, and therefore, smoothing techniques have to be adopted. Second, strain estimation does not exploit the original RF data. It rather relies solely on the noisy displacement field. In this paper, a novel technique is proposed that utilizes both the displacement field and the RF frames to accurately obtain the strain estimates. The normalized cross correlation (NCC) metric between two corresponding windows around the samples of the pre- and post-compressed images is employed to generate a dissimilarity measurement. The derivative of NCC with respect to the strain is analytically derived using the chain rule. This allows an efficient minimization of the dissimilarity metric with respect to the strain using the gradient descent optimization technique. The effectiveness of the proposed method is investigated through simulation data, phantom experiments, and *in vivo* patient data. The experimental results show that exploiting the information in RF data significantly improves the strain estimates.**

***Index Terms*— Ultrasound elastography, direct strain estimation, cost function optimization, normalized cross correlation, gradient descent, liver cancer, liver ablation.**

I. Introduction

ULTRASOUND elastography is an emerging medical imaging technique that is increasingly applied to numerous diagnostic and interventional applications. It reveals mechanical properties of the tissue by calculating tissue deformation from Radio Frequency (RF) ultrasound data [1]–[3]. Several elastography techniques have been developed and successfully applied to different medical applications [4]–[6]. Generally, these methods can be classified into quasi-statistic and dynamic elastography. In quasi-static elastography, slow tissue deformations are measured using ultrasound. These deformations can be simply differentiated to estimate strain, or used in an inverse problem formulation to calculate tissue elasticity modulus [7], [8]. In dynamic elastography, wave propagation is monitored using ultrasound, and quantitative measurements of mechanical properties of tissue are provided. Recent reviews of dynamic elastography methods can be found in [9]–[11]. In this paper, we focus on free-hand quasi-static strain imaging, wherein the small hand tremor can generate enough deformation in the tissue. Quasi-static strain elastography has numerous applications in image-guided operations and is inexpensive. Furthermore, the displacement and strain fields can be used to recover mechanical properties of tissue [7], [8].

Numerous methods have been proposed for displacement estimation from RF data. Window-based methods are arguably the most common displacement estimation technique, wherein RF data is divided into several small windows, and the displacement of each window is estimated using either phased-based or amplitude-based techniques. In phased-based schemes, the phase information in RF data is used for fast displacement estimation [12]. Amplitude-based techniques use cross correlation (CC) or normalized cross correlation (NCC) to find the tissue displacement [1], [2], [13]–[16]. In these methods, a tradeoff is made between better spatial resolution (with small windows) and better accuracy (with large windows). A recent amplitude-based technique finds level sets of CC to calculate accurate 2D displacement estimates [17]. Optimization of a cost function is another popular category for displacement estimation [2], [18]–[21]. An example of this is dynamic programming analytical minimization (DPAM) technique [3], which calculates the strain at each sample of the RF data. Here, a cost function that incorporates both the RF data and prior information of displacement continuity has been proposed for the estimation of a 2D displacement field. Once the displacement field is estimated, a spatial derivative operator is applied to calculate a strain image.

Manuscript received December 1, 2016; revised March 13, 2017; accepted March 14, 2017. Date of publication April 6, 2017; date of current version June 1, 2017. This research was funded by NSERC Discovery Grants RGPIN-2015-04136 and RGPIN-06623. *Asterisk indicates corresponding author.*

M. Omidyeganeh and Y. Xiao are with the Electrical Engineering Department, Concordia University, Montreal, QC H3G 1M8, Canada, and also with the Perform Centre, Concordia University, Montreal, QC H4B 1R6, Canada.

M. O. Ahmad is with the Electrical Engineering Department, Concordia University, Montreal, QC H3G 1M8, Canada.

*H. Rivaz is with the Electrical Engineering Department, Concordia University, Montreal, QC H3G 1M8, Canada, and also with the Perform Centre, Concordia University, Montreal, QC H4B 1R6, Canada (e-mail: hrivaz@ece.concordia.ca).

Digital Object Identifier 10.1109/TMI.2017.2685522

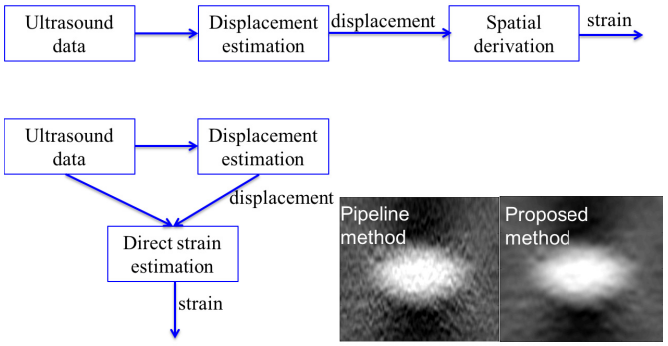

Fig. 1. The pipeline framework (top row) and the proposed scheme (bottom left). Bottom right provides a comparison of strain images generated using the two frameworks. The image generated using the proposed method has significantly higher quality.

The above methods follow a pipeline paradigm that consists of two steps of displacement estimation followed by strain estimation (Figure 1). They estimate the strain by performing spatial derivative of the displacement field, which amplifies the noise. Thus, a least squares estimation of the strain is commonly performed, which reduces the spatial resolution. The other disadvantage of these pipeline methods is that they do not exploit the RF data in the strain estimation step, and utilize only the noisy displacement field to calculate the strain. However, the RF data contains significant information that can be utilized to improve strain estimation.

Another group of the strain estimation techniques perform direct strain estimation without computing the gradient of the displacement field. These direct methods usually apply local/global adaptive temporal stretching of the signals in the time or frequency domain to calculate the strain. In time domain, Alam *et al.* [22] used the stretching factor that varies in each iteration to maximize cross-correlation (CC) to compute the strain image. In [23] and [24], a two-step method is proposed to use optical flow with local warping to compute displacements and strain simultaneously. To compensate for the signal de-correlation due to non-axial motion of tissue scatterers, Hussain *et al.* [25] proposed a direct average strain estimation (DASE) method using the weighted nearest neighbour method. Based on this method, the same group later incorporated a lesion edge preservation technique in the strain determining cost function to improve the lesion boundary definition [25], [26]. As for the techniques in frequency domain, in [27], power spectrum shift is estimated with CC to estimate the strain image, and the method is demonstrated to perform better for small strains than using spectral centroid shift [28]. Alam *et al.* [29] introduced a novel technique that estimates local strain by maximizing the spectral correlation between the pre- and post-compression echo signals using iterative frequency-scaling of the latter. With the aim of better estimating the strain for fluid-filled lesions, Nahiyan and Hasan [30] proposed a hybrid method, where a kernel-based method is applied to strain estimation of the liquid region, and a modified version of the direction strain estimation technique introduced in [31] is used for the solid region. Direct strain estimation in frequency domain can also be achieved through phase-based approaches, where the strain is modelled as a function of phase [32], [33]. Bae and Kim [32] performed direct strain estimation from the phase of the temporal and spatial correlation function of the baseband signals in pre- and post-compression frames. In [33], the phases of zero-lag cross-correlation of the pre- and stretched post-compression analytic signals are computed, and the strain is derived from a phase-versus-strain function employing secant algorithm. We compare the performance of our proposed method to four recent methods [1], [3], [23], [30], and show that it outperformed all four methods while being suitable for real-time implementation.

In this work, we propose a direct strain estimation method that uses both the initial RF data and the calculated displacement field to estimate a high quality and accurate strain image in a unified framework (Figure 1). NCC is used to calculate the similarity between two windows corresponding to the pre- and post-compression RF images. A dissimilarity metric is defined based on NCC between these two windows, and the desired stretching factor is the one that minimizes this cost function. To allow fast strain estimation, we analytically derive the derivative of the dissimilarity metric with respect to the strain using the chain rule, and therefore, can use an efficient gradient-based optimization method.

We demonstrate that the proposed cost function is convex in the vicinity of the global minimum using simulation data as well as phantom and *in-vivo* experiments. The estimated strain images from phantom experiments prove the high efficiency of our idea, especially in low strain values.

This paper consists of four sections. In Section II, the proposed method is described. Section III contains the simulation results. Also, the clinical study and the phantom trials are illustrated in Section III. Finally, the paper is concluded in Section IV.

II. Methods

Ultrasound elastography can be formulated as an optimization problem with tissue displacement as the unknown variable. Assume we have RF signals, I_{f} and I_{m} from the pre- and post-compression images, respectively, each of size $p \times q$. Subscripts f and m refer to fixed and moving images respectively, which are captured during the freehand palpation. For each point $X = (x_f, y_f)$ in the frame I_f, there is a displacement vector $D = (d_l(X), d_a(X))$, where $d_l(X)$ and $d_a(X)$ denote the lateral and axial displacements of the point X in the frame I_f, respectively.

Consider a window, $W_f(X)$, of the size $l_r \times l_c$ with the center X in the image I_f. The goal is to find $\varepsilon_a(X)$ and $\varepsilon_l(X)$, the axial and the lateral strain measures of the point X in the image I_f such that a dissimilarity measure between $W_f(X)$ and its corresponding window in the image I_m, $W_m(X+D)$ is minimized. The axial and the lateral directions and the relation between two ultrasound images are illustrated in Figure 2.

The lateral and axial strains are calculated by finding the optimal values ε_l and ε_a as outlined in Figure 3. First, a brief summary of the previous work used here to calculate the displacement fields [3] is provided in the next section. The dissimilarity measure is then described, and the optimization algorithm is introduced.

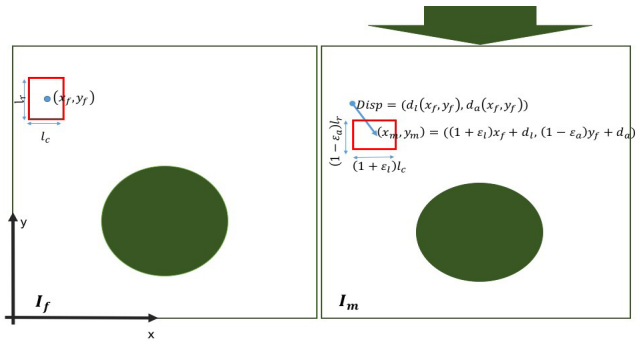

Fig. 2. Axial and lateral directions. The sample point (x_f, y_f) in the left image has moved by $D = (d_l(x_f, y_f), d_a(x_f, y_f))$ and corresponds to the point (x_m, y_m) in the right image after compressing the probe. $d_l(x_f, y_f)$ and $d_a(x_f, y_f)$ represent the lateral and axial displacements, respectively.

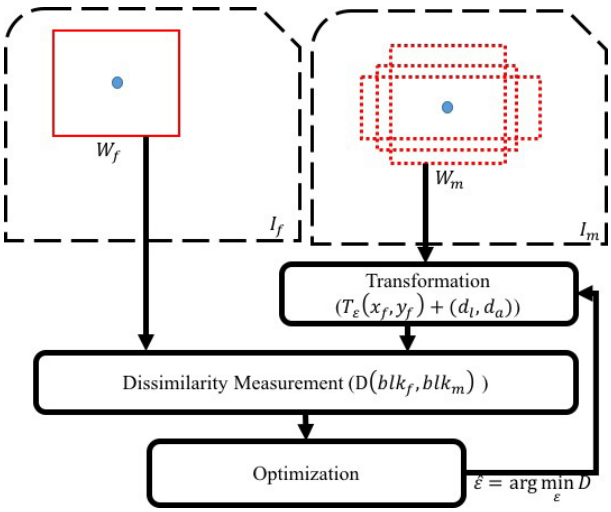

Fig. 3. The proposed iterative scheme for direct strain estimation.

A. Estimation of Displacement Fields

The axial and the lateral displacement fields are calculated by employing the 2D dynamic programming (DP) and analytic minimization (AM) algorithms [3], [19], wherein a regularized cost function is optimized to estimate the displacement field. The cost function considers both the similarity between the pre- and post-compression ultrasound images as well as a prior based on the continuity of the displacement fields. It first computes the integer axial and lateral displacement field of a seed-line using DP, and then uses the AM method to estimate a fine subpixel displacement field. The outcome of this step is the axial and lateral displacement matrices, $D_a = [d_a(x_f, y_f)]_{p\times q}$ and $D_l = [d_l(x_f, y_f)]_{p\times q}$, where $x_f = 1, 2, \ldots, p$, $y_f = 1, 2, \ldots, q$. Thus, for each point $X_f = (x_f, y_f)$ in the pre-compression image I_f, there is a point X_m in the post-compression image, I_m, that is defined as

$$\begin{aligned} X_m &= (x_m, y_m) \\ &= (x_f, y_f) + (d_l(x_f, y_f), d_a(x_f, y_f)). \end{aligned} \tag{1}$$

The DPAM technique calculates the axial and lateral displacement fields simultaneously with subsample accuracy. We now propose the new direct strain estimation technique.

B. Dissimilarity Measure

Cross correlation is a common similarity measure to estimate the level of correspondence between two signals. For two windows W_1 and W_2 of size $l_c \times l_r$, CC is calculated as

$$\begin{aligned} &CC(W_1, W_2) \\ &= \sum_{i=1}^{l_c}\sum_{j=1}^{l_r} W_1(i,j)\, W_2(i,j) = < W_1, W_2 > . \end{aligned} \tag{2}$$

The CC metric has some disadvantages. The range of the calculated CC depends on the window size [34]. It is also not invariant to variations in the image amplitude resulting by different ultrasound acquisition conditions. Therefore, we have employed NCC as our similarity metric. NCC is, in fact, the dot product of two normalized image windows, given by

$$\begin{aligned} &NCC(W_1, W_2) \\ &= \sum_{i=1}^{l_r}\sum_{j=1}^{l_c} \hat{W}_1(i,j)\, \hat{W}_2(i,j) = < \hat{W}_1, \hat{W}_2 > \\ \hat{W}_1 &= \frac{W_1 - \bar{W}_1}{\sqrt{\sum_{i=1}^{l_c}\sum_{j=1}^{l_r}(W_1(i,j) - \bar{W}_1)^2}} \\ \hat{W}_2 &= \frac{W_2 - \bar{W}_2}{\sqrt{\sum_{i=1}^{l_c}\sum_{j=1}^{l_r}(W_2(i,j) - \bar{W}_2)^2}} \\ \bar{W}_1 &= \frac{1}{l_c l_r}\sum_{i=1}^{l_c}\sum_{j=1}^{l_r} W_1(i,j) \\ \bar{W}_2 &= \frac{1}{l_c l_r}\sum_{i=1}^{l_c}\sum_{j=1}^{l_r} W_2(i,j). \end{aligned} \tag{3}$$

Thus, the dissimilarity metric between a pair of blocks of RF data, W_1 and W_2, can be obtained as

$$D = -NCC^2(W_1, W_2) = -CC^2\left(\hat{W}_1, \hat{W}_2\right), \tag{4}$$

where the negative sign makes D a dissimilarity measure, and NCC is squared to make the computation of the derivative of D simpler [35]. The maximum amount of the dissimilarity measure is zero, which occurs if the two blocks have no intensity correlation, and the minimum value is -1 if the intensities of two blocks have a linear relationship.

C. Optimization Model

The goal is to determine the amount of expansion or compression of each point of the tissue that minimizes D. To do so, we consider a window, W_f, of size $l_c \times l_r$ around the point (x_f, y_f), and find the optimal size for the window around the corresponding point (x_m, y_m) in the image I_m. Let this optimal size be $(1+\varepsilon_l)\, l_c \times (1-\varepsilon_a)\, l_r$, where ε_a and ε_l are, respectively, axial and lateral strains. To define NCC between these two corresponding windows and to find the optimum ε_l and ε_a, W_m is resized to $l_c \times l_r$ by linear

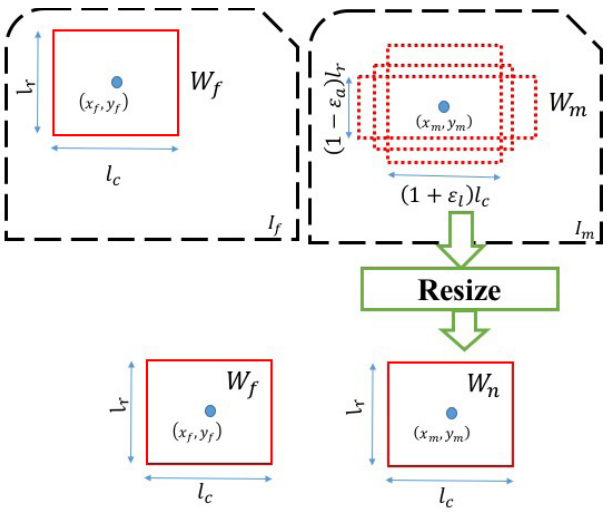

Fig. 4. Two corresponding windows from pre- and post-deformation RF images to be compared.

interpolation and the new window, W_n, is computed (Figure 4). The dissimilarity between W_f and W_n is given by

$$D = -NCC^2 = -\frac{\left(\sum_{i=1}^{l_c}\sum_{j=1}^{l_r}\left(W_f(i,j)-\bar{W}_f\right)\left(W_n(i,j)-\bar{W}_n\right)\right)^2}{\sum_{i=1}^{l_c}\sum_{j=1}^{l_r}\left(W_f(i,j)-\bar{W}_f\right)^2\sum_{i=1}^{l_c}\sum_{j=1}^{l_r}\left(W_n(i,j)-\bar{W}_n\right)^2}. \tag{5}$$

In other words, given $X_f = (x_f, y_f)$ in I_f and $X_m = (x_m, y_m)$ in I_m, we are looking for the transformation parameter $\varepsilon = (\varepsilon_l, \varepsilon_a)$. Since our windows are small, we can assume ε is constant within each window. Therefore,

$$\begin{aligned} X_m &= T(X_f) \\ x_m &= (1+\varepsilon_l)\,x_f + d_l \\ y_m &= (1-\varepsilon_a)\,y_f + d_a \\ x_f &= \frac{x_m - d_l}{(1+\varepsilon_l)} \\ y_f &= \frac{y_m - d_a}{(1-\varepsilon_a)}. \end{aligned} \tag{6}$$

Given the current transformation parameter, ε, the iterative optimization method finds an incremental $\Delta\varepsilon$, so that the new transformation parameter, $\varepsilon+\Delta\varepsilon$, reduces the dissimilarity measurement. To perform fast optimization, we use the chain rule to find an analytic expression for the gradient as

$$\begin{aligned} \frac{\partial D}{\partial \Delta\varepsilon_a} &= \frac{\partial D}{\partial W_m}\cdot\frac{\partial W_m}{\partial y_m}\cdot\frac{\partial y_m}{\partial \Delta\varepsilon_a} \\ \frac{\partial D}{\partial \Delta\varepsilon_l} &= \frac{\partial D}{\partial W_m}\cdot\frac{\partial W_m}{\partial x_m}\cdot\frac{\partial x_m}{\partial \Delta\varepsilon_l}. \end{aligned} \tag{7}$$

From (6), we have:

$$\frac{\partial x_m}{\partial \Delta\varepsilon_l} = x_f,\ \frac{\partial y_m}{\partial \Delta\varepsilon_a} = -y_f, \tag{8}$$

where $\frac{\partial W_m}{\partial y_m}$ and $\frac{\partial W_m}{\partial x_m}$ are the image gradients. W_n is the scaled version of W_m and by some manipulations, $\frac{\partial D}{\partial W_m}$ can be considered equal to $\frac{\partial D}{\partial W_n}$ and calculated as (9), as shown at the bottom of this page.

In (7), the gradients of the points of the moving window should be calculated. This involves the interpolation of the moving window after each iteration. To solve this problem, the image gradient can be computed at on-grid points of the fixed window employing the technique proposed and utilized in [3], [36], and [37]. It is proved in [38] that the final results of calculating gradients on the fixed and moving images are the same, the former being computationally more efficient. Hence, we write the chain rule as

$$\begin{aligned} \frac{\partial D}{\partial \Delta\varepsilon_a} &= \frac{\partial D}{\partial W_f}\cdot\frac{\partial W_f}{\partial y_f}\cdot\frac{\partial y_f}{\partial \Delta\varepsilon_a} \\ \frac{\partial D}{\partial \Delta\varepsilon_l} &= \frac{\partial D}{\partial W_f}\cdot\frac{\partial W_f}{\partial x_f}\cdot\frac{\partial x_f}{\partial \Delta\varepsilon_l}. \end{aligned} \tag{10}$$

Based on (6), we have

$$\begin{aligned} \frac{\partial x_f}{\partial \Delta\varepsilon_l} &= -\frac{x_m - d_l}{(1+\Delta\varepsilon_l+\varepsilon_l)^2} = -\frac{x_f}{(1+\Delta\varepsilon_l+\varepsilon_l)} \\ \frac{\partial y_f}{\partial \Delta\varepsilon_a} &= \frac{y_m - d_a}{(1-\Delta\varepsilon_a-\varepsilon_a)^2} = \frac{y_f}{(1-\Delta\varepsilon_a-\varepsilon_a)}, \end{aligned} \tag{11}$$

where $\frac{\partial W_f}{\partial y_f}$ and $\frac{\partial W_f}{\partial x_f}$ are the vertical and horizontal gradients of the image, and the first factor of (10) is defined as

Note that Eqs (7), (9), (10) and (12), as shown at the top the next page, all produce scalar values.

D. Iteration Equation

Letting $\frac{\partial D}{\partial \Delta\varepsilon_a}$ and $\frac{\partial D}{\partial \Delta\varepsilon_l}$ to be the derivatives of the dissimilarity function with respect to the unknown variables ε_a and ε_l,

$$\frac{\partial D}{\partial W_n} = -2\Bigg(\frac{\sum_{i=1}^{l_c}\sum_{j=1}^{l_r}\left(W_f(i,j)-\bar{W}_f\right)\left(W_n(i,j)-\bar{W}_n\right)}{\sum_{i=1}^{l_c}\sum_{j=1}^{l_r}\left(W_f(i,j)-\bar{W}_f\right)^2\sum_{i=1}^{l_c}\sum_{j=1}^{l_r}\left(W_n(i,j)-\bar{W}_n\right)^2}\left(W_f-\bar{W}_f\right) - \frac{\sum_{i=1}^{l_c}\sum_{j=1}^{l_r}\left(W_f(i,j)-\bar{W}_f\right)\left(W_n(i,j)-\bar{W}_n\right)}{\sum_{i=1}^{l_c}\sum_{j=1}^{l_r}\left(W_n(i,j)-\bar{W}_n\right)^2}\left(W_n-\bar{W}_n\right)\Bigg). \tag{9}$$

$$\frac{\partial D}{\partial W_f} = -2\Big(\frac{\sum_{i=1}^{l_c}\sum_{j=1}^{l_r}\left(W_f(i,j)-\bar{W}_f\right)\left(W_n(i,j)-\bar{W}_n\right)}{\sum_{i=1}^{l_c}\sum_{j=1}^{l_r}\left(W_f(i,j)-\bar{W}_f\right)^2\sum_{i=1}^{l_c}\sum_{j=1}^{l_r}\left(W_n(i,j)-\bar{W}_n\right)^2}\left(W_n-\bar{W}_n\right) - \frac{\sum_{i=1}^{l_c}\sum_{j=1}^{l_r}\left(W_f(i,j)-\bar{W}_f\right)\left(W_n(i,j)-\bar{W}_n\right)}{\sum_{i=1}^{l_c}\sum_{j=1}^{l_r}\left(W_f(i,j)-\bar{W}_f\right)^2}\left(W_f-\bar{W}_f\right)\Big). \tag{12}$$

the optimization problem at each point of the image I_f is defined as

$$\begin{aligned} C &= D\left(I_f(X), I_m(T_\varepsilon(X))\right) \\ \hat{\varepsilon} &= \arg C \\ \varepsilon &= (\varepsilon_l, \varepsilon_a). \end{aligned} \tag{13}$$

We use the gradient descent scheme to optimize this cost function. Since we have analytically derived the derivative of the cost function, the gradient descent technique would be very efficient. At each iteration, the algorithm looks for the minimum in the negative direction of the gradient at each point. Consequently, at each iteration, ε_l and ε_a are updated as

$$\varepsilon_{t+1} = \varepsilon_t + \alpha\ \Big(\frac{\partial D}{\partial \Delta\varepsilon_l}, \frac{\partial D}{\partial \Delta\varepsilon_a}\Big), \tag{14}$$

with $0 < \alpha < 1$ a user-defined constant. The value of the step size, α, can be changed in each iteration. The gradient descent algorithm with fixed step size will converge if the function is convex and differentiable [38], [39]. Varying the step-size, however, allows a faster convergence. The idea is to select large step sizes far from the minimum and small step sizes close to it [38], [39]. Two examples that employ variable step size techniques are the exact line search and Brazilai-Browein schemes. To avoid the unnecessary complexity, we use an *ad-hoc* idea and refined the step size at each iteration as

$$\alpha_{a_t} = \alpha_{a_{t-1}} + \rho\left(sign\Big(\frac{\partial D}{\partial \Delta\varepsilon_a}(t)\Big) sign\Big(\frac{\partial D}{\partial \Delta\varepsilon_a}(t-1)\Big)\right), \tag{15}$$

where $0 < \rho < 1$. The step size is decreased if the sign of the derivative of the cost function changes and increased if the sign remains the same.

In the next section, we will show that the proposed cost function is convex and study the results of the method on the simulated, phantom and clinical data.

III. Experimental Results

Simulation, phantom and *in-vivo* trials are employed to validate the proposed scheme. The displacement fields are calculated using DPAM implemented in Matlab Mex functions [3], which is available online. The proposed algorithm is implemented in Matlab and takes 6.9 sec on a 2.7 GHz Intel Core i5 processor. The algorithm can be implemented in Mex functions for real-time performance.

The image strain is constructed after estimating the ε values at each point by optimizing the cost function in (13). The dissimilarity metric is defined based on NCC and the gradient descent algorithm is used to find the minimum of the function. The gradient of the cost function is computed employing (12).

It is well known that ultrasound point spread function is very wide in the lateral direction, and therefore, lateral resolution is significantly lower than axial resolution. Therefore we do not show lateral strain images. Nevertheless, lateral displacement and strain can be used to improve the quality of elasticity reconstruction techniques [7], [29], [40].

We compare our results with the results of the least square (LSQ) based [1] and Kalman filter (KF) based methods in [3]. The strain images are depicted in the same range to make them comparable. To assess the performance of the proposed algorithms two metrics are employed: the signal to noise ratio (SNR) and the contrast to noise ratio (CNR) [41]. These two metrics are calculated as

$$\begin{aligned} SNR &= \frac{S}{R} = \frac{\bar{s}}{\sigma} \\ CNR &= \frac{C}{N} = \sqrt{\frac{2\left(\bar{s_b}-\bar{s_t}\right)^2}{\sigma_b^2+\sigma_t^2}}, \end{aligned} \tag{16}$$

where, $\bar{s_b}$ and $\bar{s_t}$ denote the mean value of the background and target of the strain image, respectively; σ_b^2 and σ_t^2 represent the variances of the background and the target, and $\bar{s}$ and σ are the mean and variance of a window in the strain image.

A. Simulation Results

The proposed technique is verified employing a simulated phantom experiment described in [3]. The phantom is assumed to be isotropic for finite element simulation. The phantom has a soft inclusion. The size of the phantom is $36 \times 10 \times 25$ mm and 1.4×10^5 scatterers with Gaussian scattering strengths are distributed uniformly in the phantom. Field II software is used for simulating ultrasound images [42]. The soft lesion is spherical with the diameter of 10 mm, and is oriented vertical to the image plane. A uniform compression is applied on the phantom vertically, causing the phantom to be deformed. The displacement field is computed employing ABAQUS, where the Poisson ratio is set to 0.49 [43].

First, to investigate the convexity of the dissimilarity metric, a window W_f of size 51x21 is selected in the

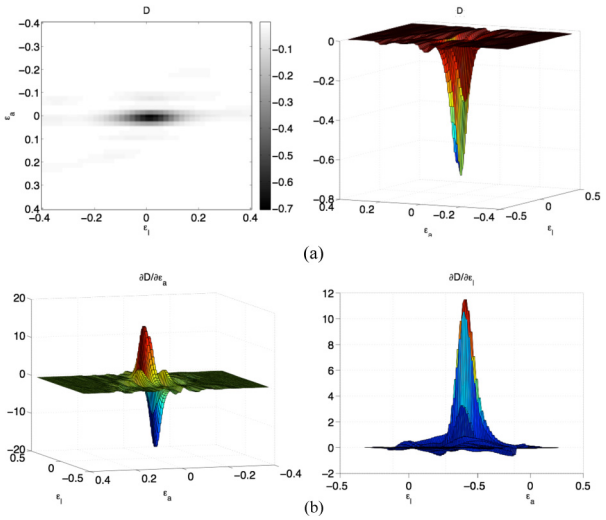

Fig. 5. Results of the simulation experiment. (a)Dissimilarity measure D for different values of ε_a and ε_l for a simulated data window. (b) Derivatives of D with respect to ε_a and ε_l.

TABLE I
THE SNR AND CNR VALUES OF THE STRAIN IMAGES SHOWN IN FIGURE 7

	LSQ-based method [1]	KF-based method [3]	Optical-flow-based method [23]	Hybrid method [30]	Proposed method
SNR	24.89	25.49	7.63	20.31	**29.26**
CNR	9.99	10.38	6.42	9.23	**10.55**

pre-compressed image. The corresponding window in the post-compressed image is then selected using the displacement field calculated by DPAM technique [3]. The dissimilarity metric D is calculated for different values of the variables ε_a and ε_l. And the derivatives of D with respect to ε_a and ε_l are calculated. Results are illustrated in Figure 5. It is seen from this figure that the dissimilarity function has a global minimum and its derivatives are zero at this minimum.

We also plot the mean square error (MSE) versus the step size used in the gradient descent algorithm for ε_a and ε_l, as shown in Figure 6. As seen from this figure, both curves have a small value at $\alpha = 10^{-5}$. Thus, in this work this value is selected as the step size.

Next, the strain image is estimated by employing the proposed algorithm. The result is shown in Figure 7 and is compared to those obtained by using the LSQ-based [1], KF-based [3], optical-flow-based [23] and hybrid [30] methods. This figure shows the high quality of the strain images estimated with the proposed method. The maximum CNR gained with our method, calculated by the step size value equal to 10^{-5} is 20.4. The CNR and SNR values are given in Table 1. For comparison, we employed the procedure introduced in [23] without median filtering. The results can be substantially improved using a median filter.

Besides SNR and CNR, we also computed the strain ratios to evaluate the accuracy of strain estimation for different methods. The values are compared to the true stiffness ratio

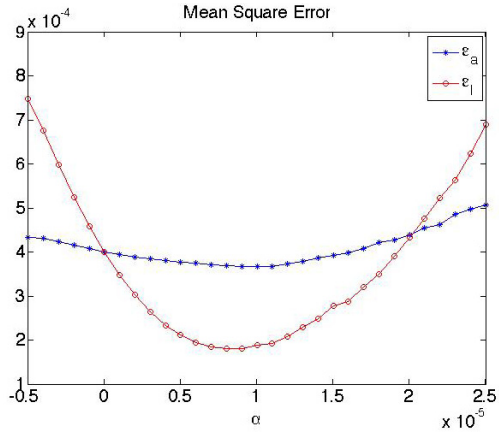

Fig. 6. Mean square error (MSE) versus GD step size (α) used for ε_a and ε_l in the simulation experiment.

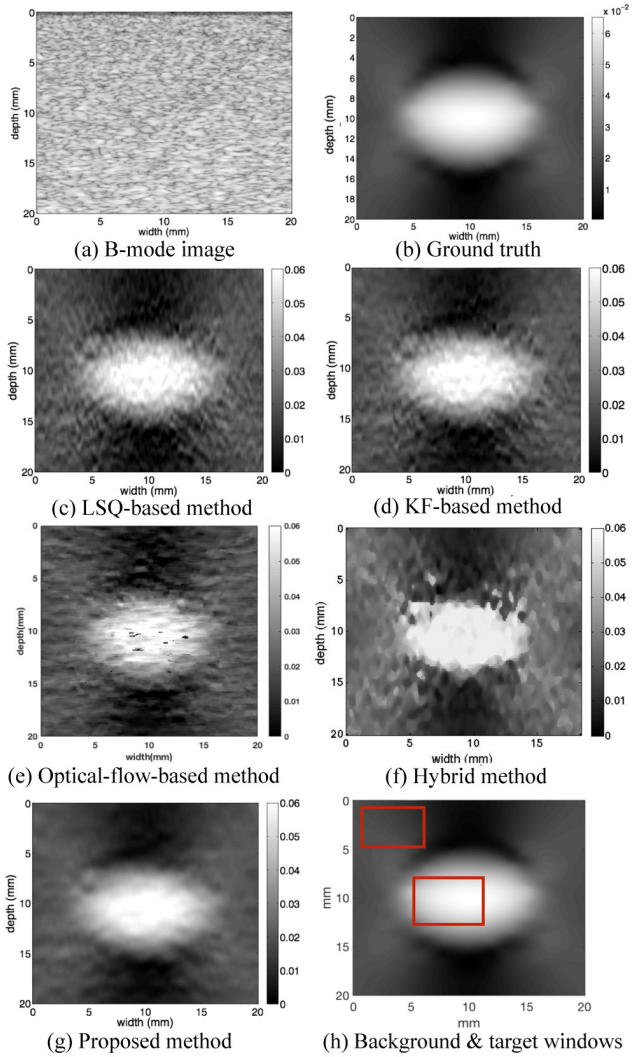

Fig. 7. Axial strain images of the FEM phantom. The background and target windows for SNR & CNR analysis are overlaid on the ground truth strain image in (h).

of the phantom, which is 3.72. The values of strain ratios are evaluated at 3.31, 3.30, 6.83, 6.55, and 3.38 for the LSQ [1], KF-based [2], optical-flow-based [23], hybrid [30]

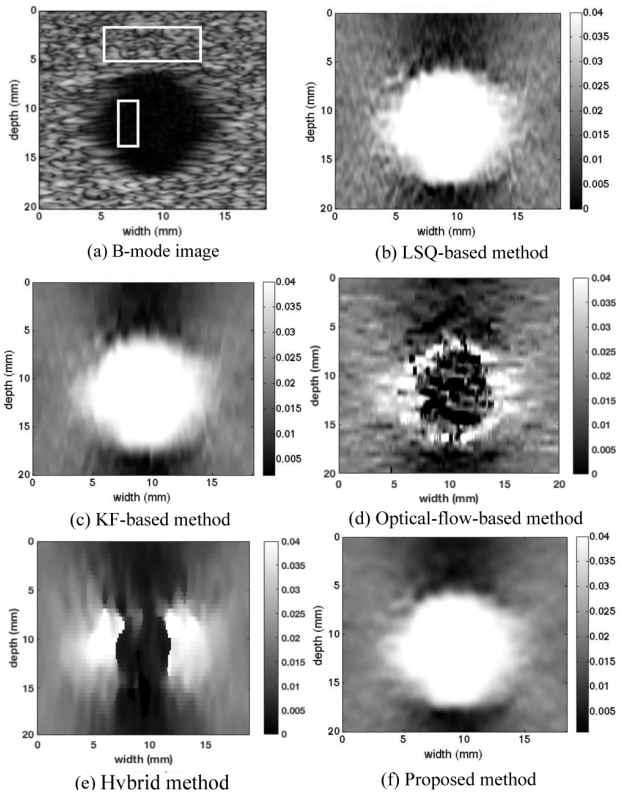

Fig. 8. Axial strain images of the FEM cyst phantom. The background and target windows for SNR & CNR analysis are shown in part (a).

TABLE II
THE SNR AND CNR VALUES OF THE STRAIN IMAGES SHOWN IN FIGURE 8

	LSQ-based method [1]	KF-based method [3]	Optical-flow-based method [23]	Hybrid method [30]	Proposed method
SNR	19.74	17.59	2.24	8.65	**29.26**
CNR	9.55	9.43	0.71	10.05	**10.55**

and proposed methods, respectively. The proposed method most accurately predicts the strain ratio.

To test the performance of our method for cysts, we simulate a cyst phantom using Field II and ABAQUS finite element software packages, and estimated the strain with LSQ-based method [1], KF-based method [3], optical-flow-based method [23], our proposed method, and the hybrid method by Nahiyan and Hasan [30], which is specially designed for estimating strains of cysts. The cyst part of the phantom does not contain any scatterers, and the rest of the phantom consists of fully developed speckles wherein more than 10 scatterers are distributed in each resolution cell. The size of the phantom is 20×20×10 mm, and the cyst is spherical with a diameter of 10 mm. The comparison of different methods is shown in Figure 8, and the SNR and CNR of these results are shown in Table 2. Note that both the optical-flow-base and hybrid methods (Fig. 8 (d) and (f)) show poor performance in the middle of the cyst lesion. We have selected the target window as shown in part (a) to avoid these regions.

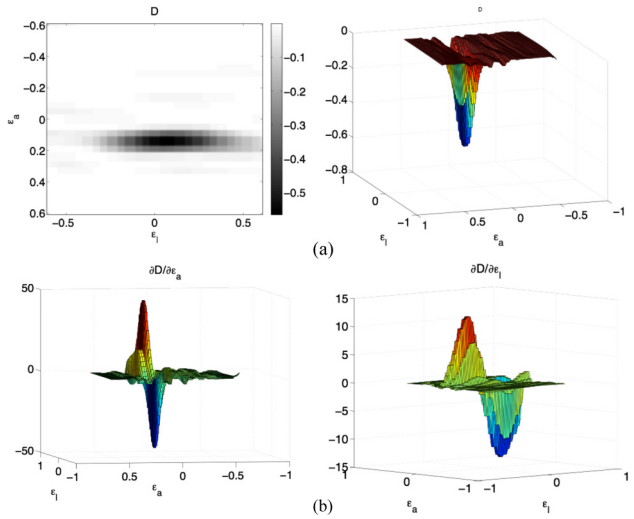

Fig. 9. Results of the phantom experiment. (a)Dissimilarity measure D for different values of ε_a and ε_l. (b) Derivatives of D with respect to ε_a and ε_l.

TABLE III
SNR AND CNR OF THE STRAIN IMAGES SHOWN IN FIGURE 10. SNR IS CALCULATED FOR THE BACKGROUND WINDOW IN FIGURE 11 (A)

	LSQ-based method [1]	KF-based method [3]	Optical-flow-based method [23]	Hybrid method [30]	Proposed method
SNR	13.6	21.7	9.66	8.28	**26.9**
CNR	5.9	11.1	1.03	6.12	**11.7**

B. Phantom Results

We now verify the effectiveness of the proposed technique using experimental data from a tissue mimicking CIRS phantom (Norfolk, VA) with a Siemens Antares ultrasound machine (Issaquah, WA). The CIRS elastography phantom has been compressed axially by a linear stage. The captured RF images of the pre- and post-compression are used to calculate the displacement and strain fields. The Young's elasticity modulus of the compressed lesion and background are 56 kPa and 33 kPa, respectively.

To study the convexity of the dissimilarity metric D for phantom data, D is calculated for different values of the variables ε_a and ε_l, for a window of size 51x11, and the derivatives of D with respect to ε_a and ε_l are calculated and plotted in Figure 9; These plots illustrate that there is a global minimum in the cost function and the derivatives are continuous and cross zero at the minimum.

The calculated strain image is depicted in Figure 10. The axial strain image scales are the same for two images. The step size is chosen to be $\alpha = 10^{-5}$, and the size of each window is selected 71×5. CNR and SNR results show the high efficiency of the proposed method in comparison to the LSQ-based and KF-based schemes (Table 3).

The values of CNR have been also calculated for different amounts of gradient descent step sizes, α, and shown in Figure 11(b). These values have been calculated for both variable and fixed step sizes. The CNR plots show that both

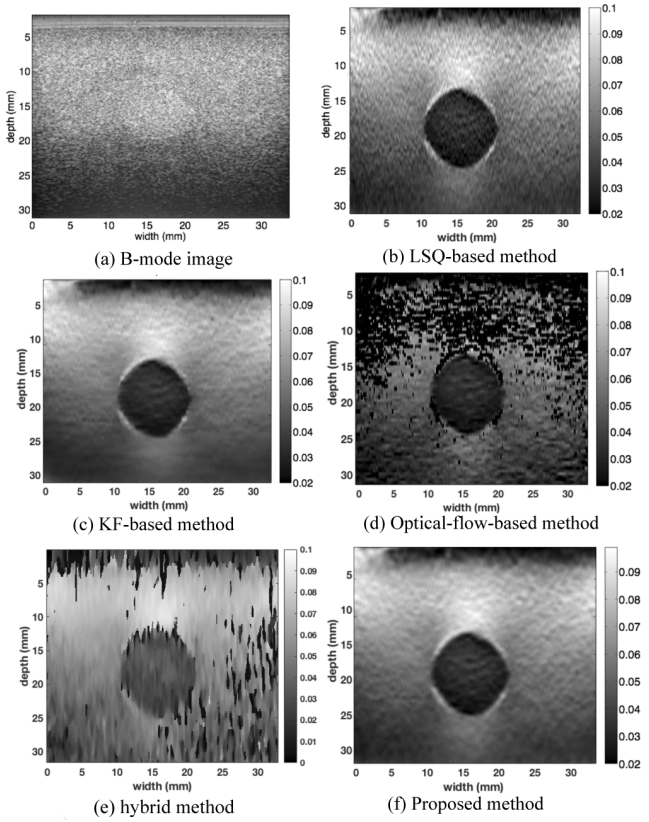

Fig. 10. Axial strain images of the phantom using different methods.

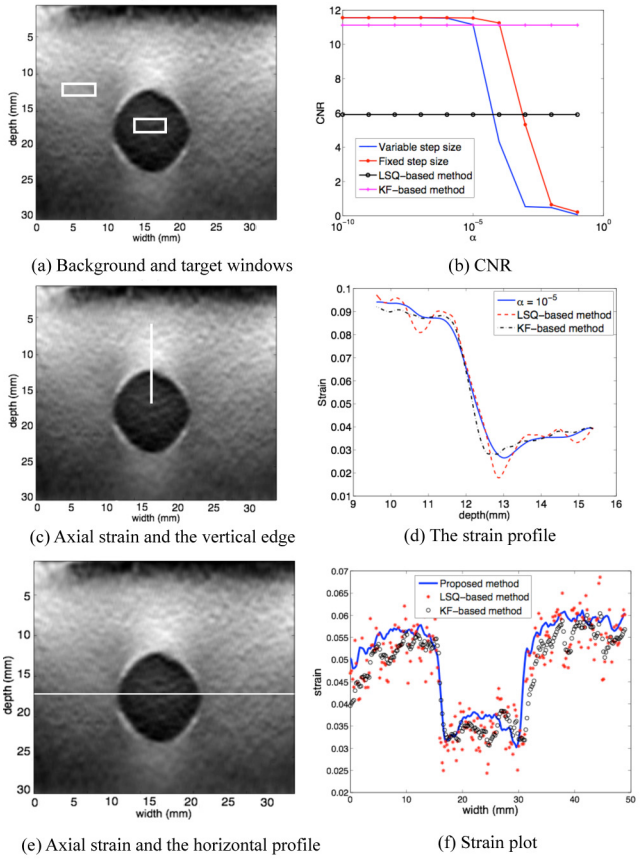

Fig. 11. Strain estimation in the phantom study. The regions of interests are marked in the strain images in (a), (c) and (e). (b) CNR versus the step size. (d) & (f). The strain profiles in the axial and lateral directions.

the fixed and the variable step sizes give the same results; however, the variable step size method requires less iterations. This result shows that even for a very large range of α, CNR undergoes negligible variations. Moreover, the strain values across a vertical edge and a lateral edge, as illustrated in Fig. 11(c) and 11(e), are computed for the proposed method as well as LSQ-based and KF-based schemes. The result is shown in Fig. 11(d) and 11(f).

To further examine the quality of the strain estimation, we also computed the strain ratios in comparison to the true stiffness ratio of the phantom, which is 1.697. The values of strain ratios are evaluated at 1.372, 1.388, 1.18, 0.44, and 1.375 for the LSQ [1], KF-based [3], optical-flow-based [23], hybrid [30], and proposed methods.

In addition to the SNR and CNR measurements, we also evaluated the spatial resolution of the image using modulation transfer function (MTF). The MTF is an established method for estimating the spatial resolution of medical imaging systems that was extended to elastography [44], and can be calculated through three steps [45], [46]. First, the edge spread function (ESF) is obtained by averaging the pixel values across the background-inclusion interface (the vertical in Figure 11.c). Then, the line spread function (LSF) is computed by differentiating the ESF; lastly, the MTF is obtained by computing the Fourier transform of the LSF and normalizing the resulting function to zero spatial frequency. The results of the MTF of the LSQ-based [1], KF-based [3], and the proposed method are shown in Figure 12. For the proposed method, we also demonstrated the impact of regularization values on

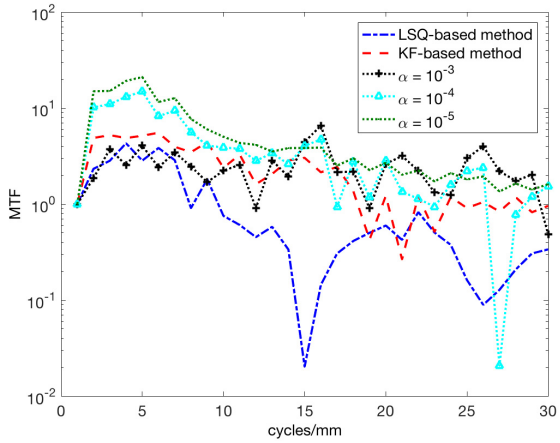

Fig. 12. Modulation transfer function (MTF) calculated from the vertical line shown in Figure 11(c) for the LSQ-based, KF-based, and the proposed methods. For the proposed methods, different regularization values.

the spatial resolution. Overall, the proposed method outperforms the other two methods, and the increasing regularization value adversely affects the spatial resolution.

In the second phantom experiment, freehand palpation of a CIRS breast elastography phantom (Norfolk, VA) is used to assess the effectiveness of the proposed technique in a range of strain levels from 1% to 11%. This phantom has a 10 mm diameter lesion which is three times harder than the

TABLE IV
SNR AND CNR OF THE STRAIN IMAGES ESTIMATED WHEN DIFFERENT STRAIN LEVELS ARE APPLIED TO THE BREAST CIRS PHANTOM. NOTE THAT CNR IS SHOWN IN SQUARE BRACKETS "[]" FOR EACH STRAIN LEVEL AND METHOD

Strain level (%)	LSQ-based method [1]	KF-based method [3]	Proposed method
1	4.3 [0.9]	3.7 [3.1]	**8.8 [7.0]**
2	3.9 [1.0]	9.8 [3.0]	**12.1 [6.5]**
3	3.2 [3.3]	10.2 [4.4]	**12.6 [5.7]**
4	3.2 [4.2]	10.6 [9.2]	**17.9 [11.2]**
5	3.3 [4.1]	16.0 [8.8]	**26.6 [10.5]**
6	3.3 [4.6]	13.8 [9.6]	**19.6 [10.7]**
7	3.3 [4.9]	11.4 [10.1]	**14.3 [11.1]**
8	3.3 [5.2]	12.9 [13.3]	**18.7 [15.7]**
9	3.3 [4.4]	6.5 [9.5]	**9.6 [12.5]**
10	1.5 [3.5]	3.9 [6.6]	**5.7 [9.0]**
11	2.3 [2.2]	2.7 [3.7]	**3.8 [5.3]**

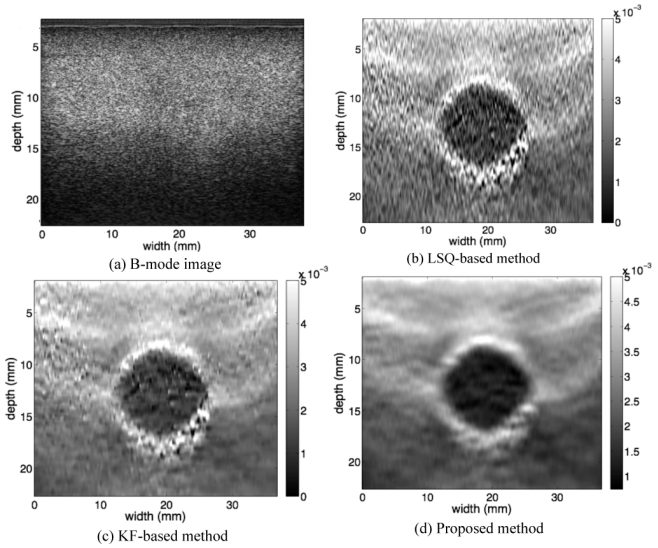

Fig. 13. Axial strain images with low strain (1%) of a CIRS breast elastography phantom.

background. We computed the SNR and CNR of the strain images estimated with the LSQ-based [1], KF-based [3], and proposed method at the strain levels of 1∼11%. As the results in Table 4 have shown, our introduced method consistently offers better performance for a large range of strain levels. Qualitatively, Fig. 13 demonstrates a comparison of the three methods when a low strain was applied to the phantom, and the proposed method gives a more visually pleasing result.

C. In-Vivo Data

To evaluate the performance of the proposed technique, ultrasound RF data from patients with liver cancer following RF ablation is used. Ultrasound data is collected using a Siemens Antares system (Issaquah, WA) with a center frequency of 6.67 MHz with a VF10-5 linear array. Full description of the data collection protocol is provided in [18].

We first investigate the convexity of the cost function, D, for different values of the variables ε_a and ε_l, for a window

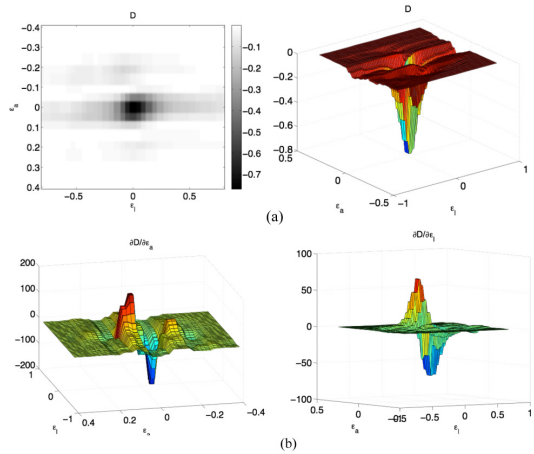

Fig. 14. Results of the *in-vivo* data. (a) Dissimilarity measure D for different values of ε_a and ε_l. (b) derivatives of D with respect to ε_a and ε_l.

size 51x11 of the pre- deformed RF image of patient 1 (Figure 14). The derivatives of D with respect to ε_a and ε_l are also shown. There is a global minimum of the cost function and the derivatives are continuous.

The strain images of three patients are shown in Figure 15. These ultrasound images are captured after RF ablation. Tissue has been compressed slightly with the ultrasound probe by the approximate frequency of 1 deformation per 2 second [3]. The B-mode scans are shown in the left column of the image. The dark shadows are caused by the thermal lesion. The strain images are computed by the proposed algorithm and are depicted in the right column of the Figure 15. The thermal lesions, which were not noticeable in the B-mode images are clear in the strain images. Post-operative computed tomography (CT) images of the three patients are also shown. An expert has visually inspected the 3D CT images to find the corresponding slice to the ultrasound images, and has delineated the ablation lesion in the CT images. The lesion outlines are overlaid on strain images to aid comparison. It should be noted that since the ultrasound probe is not tracked and liver deforms significantly during surgery, the CT image does not exactly correspond to the ultrasound image. Note that the results of the proposed method are not only smoother, but also are substantially darker in the lesion. To fully verify the robustness of our method for *in vivo* data, we obtained strain images of 20 pairs of RF images using the LSQ-based [1], KF-based, and proposed method. The CNR and the SNR values of the strain images of the three patients are given as mean±sd values in Tables 5 and 6, which show that the proposed method outperforms both LSQ and KF.

IV. DISCUSSION

There are some similarities between the direct strain estimation method by Pan *et al.* [23] and the proposed methods. In both methods, displacements are computed to facilitate direct strain estimation. While the method of Pan *et al.* [23] employs both speckle tracking and optical flow methods to obtain displacements, ours uses 2D dynamic programming and analytic minimization (DPAM) algorithms [3], [19]. The method in [23] obtains the final strain results using strain

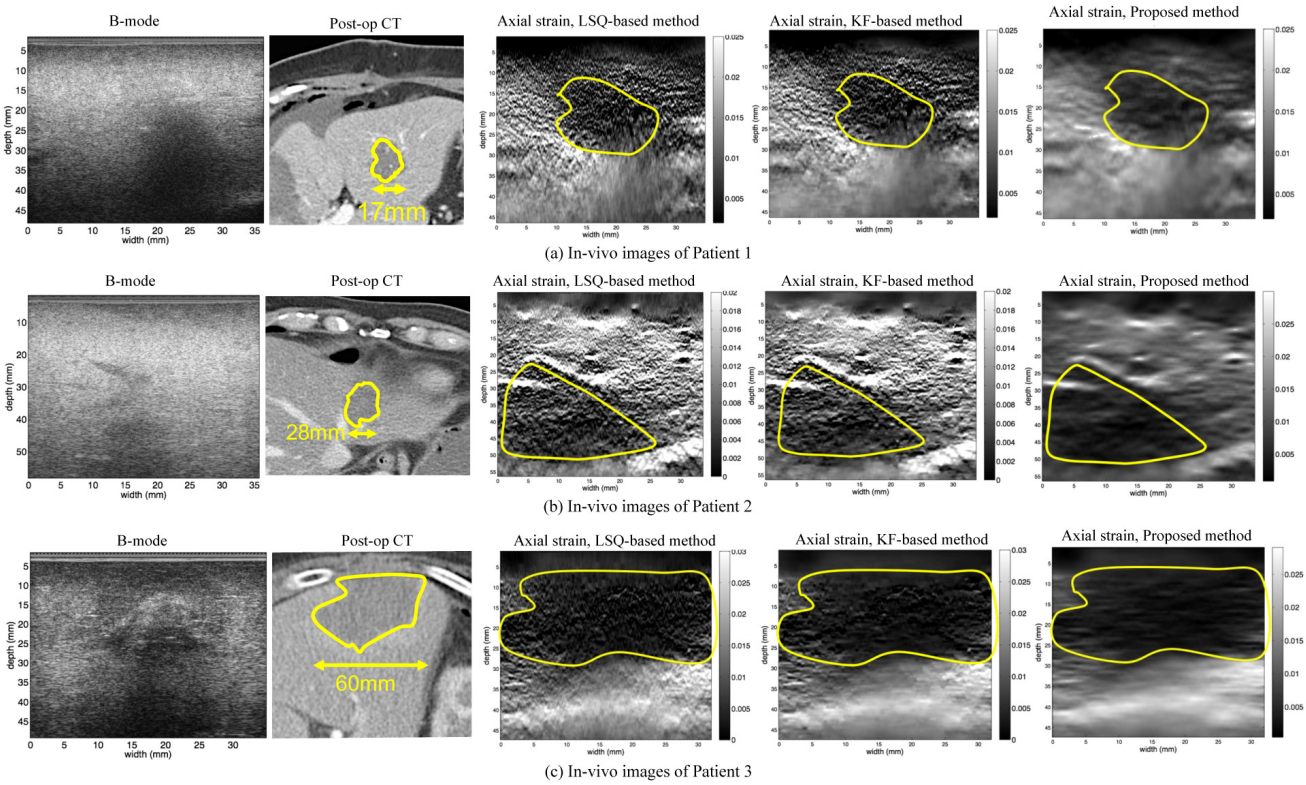

Fig. 15. *In-vivo* images of the thermal lesion of RF ablation therapy of the liver cancer. The thermal lesions are delineated manually in yellow, and are not visible in the B-mode images. The corresponding post-operative CT images with the delineated lesion boundaries are also shown.

TABLE V
THE CNR VALUES (MEAN±SD) OF THE STRAIN IMAGES COMPUTED FROM 20 PAIRS OF RF-IMAGES FOR PATIENT 1, 2 & 3. THE RF-IMAGES ARE THOSE AFTER THE ABLATION EXPERIMENTS

	LSQ-based method [1]	KF-based method [3]	Proposed method
Patient 1	1.5±1.0	2.0±1.5	**3.6±2.6**
Patient 2	1.4±0.4	1.6±0.5	**4.2±1.2**
Patient 3	2.6±1.6	2.7±1.5	**4.2±3.8**

TABLE VI
SNR VALUES (MEAN±SD) OF THE STRAIN IMAGES COMPUTED FROM 20 PAIRS OF RF-IMAGES FOR PATIENT 1, 2 & 3. THE RF-IMAGES ARE THOSE AFTER THE ABLATION EXPERIMENTS

	LSQ-based method [1]	KF-based method [3]	Proposed method
Patient 1	2.7±1.0	3.9±1.8	**5.3±2.9**
Patient 2	0.8±0.2	0.8±0.2	**1.9±0.4**
Patient 3	1.9±1.7	2.0±1.8	**2.1±1.8**

tensors and aggregation of strains estimated from two steps, and our method uses an iterative optimization approach that solves for the final results directly. However, the aggregation of strain tensors in [23] may allow the propagation and accumulation of errors at each subsampling stages, and through validation using phantom simulation, our method is shown to outperform the technique of Pan *et al.* [23]. By comparing the method in [30] to estimate strain of fluid-filled lesions, our proposed method has also shown good performance. This shows that the proposed method is capable of handling strain imaging of various lesion types. It is important to note that [30] is specifically designed for strain imaging of cysts, but due to the fact that a segmentation procedure is involved to identify the liquid-filled region, the hybrid method [30] did not perform well in comparison to our technique. This might be partially due to limitation of our simulation model, and the hybrid method of [30] might outperform our method in real experiments.

The DPAM algorithm [3] calculates the displacement field for shallow and deep regions of the image simultaneously, and typically it requires some attenuation compensation. However, the proposed method employs small windows instead of the entire image depth, and as such, does not require any attenuation compensation. If DPAM displacement field is inaccurate due to unknown attenuation coefficients, the proposed method substantially improves the strain estimates.

Most displacement estimation techniques require an explicit or implicit estimation of the gradient of the RF data. For example, in DPAM, gradient of the RF data is explicitly required for calculation of the displacement field ([3, eqs. (4) and (5)]). Therefore, strain estimation requires two gradient operations: once for estimation of displacement field from RF data, and the second time for estimation of the strain image from the displacement field. Whereas the proposed method only requires one gradient operation of the RF data in Eq. 14. Gradient operations amplify noise, and this can be considered as a reason for why the proposed method outperforms DPAM.

We employed gradient descent optimization with a dynamically changing step size to estimate the strain image.

The application of the algorithm largely benefits from the analytic formulation of the gradient of the cost function, and the dynamic step size strategy helps stabilize the optimization near the target solution without being trapped in possible local minima. In the future, we will explore other optimization methods that could potentially further improve the speed and quality of the optimization.

In addition to simulation and phantom experiments, we have also demonstrated the potential application of the proposed method in monitoring RF ablation. As currently it is not possible to monitor RF ablation to ensure that the tumour and a safety margin around it are coagulated, surgeons rather determine the ablation time based on the size of the tumour. Unfortunately, tumours that are located close to blood vessels require longer ablation because the blood vessel acts as a heat sink, and therefore the tumour may not be fully coagulated. As a result, RF ablation surgeries show high recurrence rate of up to 84% [47]. We have shown that the ablation lesions are better visualized in the strain images. We further showed that the proposed method provides better SNR and CNR values, which may help improve the outcome of the surgery.

We have demonstrated that the proposed cost function is convex in simulation, phantom and *in-vivo* experiments. Furthermore, the results of Fig. 7, 8 and 10 show that the proposed method converges to the correct solution for strain values ranging from 0 to 10%. This is a very wide strain range and most clinical applications require a much smaller strain range. Therefore, the proposed solution can be reliably used in a wide variety of clinical applications.

Although the proposed method estimates both axial and lateral strains, the quality of the lateral strain is much lower and is therefore not presented in this work. Estimation of more accurate lateral strain images is a subject of future work. Another limitation of the proposed method is that it is only tested on images obtained with traditional beamforming, and its application to new techniques such as plane-wave imaging [9] is a subject of future work. The proposed method has been developed for linear array transducers, and its adoption for curvilinear transducers is a subject of future work. Finally, there is a growing interest in development of 2D transducers that are suitable for 3D ultrasound imaging. Volumetric 3D images require significantly more computations for strain estimation. A strength of our method is its computational efficiency, and as such, it is highly suitable for 3D elastography.

V. Conclusion

In this paper, a direct strain estimation technique has been proposed. Corresponding points of two ultrasound scans are compared by considering the NCC measure of their neighborhood data. The amount of the deformation of the post-compression window is calculated using the gradient descent (GD) optimization method. The technique has been evaluated using the simulated, phantom and *in-vivo* data. The results have shown a high efficiency of the proposed technique, especially in images with low strain. These improvements are a result of exploiting the RF data for strain estimation, rather than relying solely on displacement fields.

Acknowledgement

The *in-vivo* data was collected when H. R. was a student at Johns Hopkins University. The principal investigators were Drs. Emad Boctor, Gregory Hager and Michael Choti. The authors would like to thank E. B., G. H. and M. C. for allowing them to use this data. They also thank anonymous reviewers for their constructive feedback.

References

[1] J. Ophir *et al.*, "Elastography: Ultrasonic estimation and imaging of the elastic properties of tissues," *Proc. Inst. Mech. Eng., H, J. Eng. Med.*, vol. 213, no. 3, pp. 203–233, 1999.

[2] T. J. Hall *et al.*, "Recent results in nonlinear strain and modulus imaging," *Current Med. Imag. Rev.*, vol. 7, no. 4, pp. 313–327, 2011.

[3] H. Rivaz, E. M. Boctor, M. A. Choti, and G. D. Hager, "Real-time regularized ultrasound elastography," *IEEE Trans. Med. Imag.*, vol. 30, no. 4, pp. 928–945, Apr. 2011.

[4] E. Brusseau, J. Kybic, J.-F. Déprez, and O. Basset, "2-D locally regularized tissue strain estimation from radio-frequency ultrasound images: Theoretical developments and results on experimental data," *IEEE Trans. Med. Imag.*, vol. 27, no. 2, pp. 145–160, Feb. 2008.

[5] R. Ahmed *et al.*, "Comparison of windowing effects on elastography images: Simulation, phantom and *in vivo* studies," *Ultrasonics*, vol. 66, pp. 140–153, Mar. 2015.

[6] E. Brusseau, J. Fromageau, N. G. Rognin, P. Delachartre, and D. Vray, "Investigating elastic properties of soft biological tissues," *IEEE Eng. Med. Biol. Mag.*, vol. 21, no. 4, pp. 86–94, Jul. 2002.

[7] S. R. Mousavi, A. Sadeghi-Naini, G. J. Czarnota, and A. Samani, "Towards clinical prostate ultrasound elastography using full inversion approach," *Med. Phys.*, vol. 41, p. 033501, Mar. 2014.

[8] C. Hoerig, J. Ghaboussi, and M. F. Insana, "An information-based machine learning approach to elasticity imaging," *Biomech. Modeling Mechanobiol.*, 2016, doi: 10.1007/s10237-016-0854-6.

[9] M. Tanter and M. Fink, "Ultrafast imaging in biomedical ultrasound," *IEEE Trans. Ultrason., Ferroelect., Freq. Control*, vol. 61, no. 1, pp. 102–119, Jan. 2014.

[10] J. Bamber *et al.*, "EFSUMB guidelines and recommendations on the clinical use of ultrasound elastography. Part 1: Basic principles and technology," *Ultraschall Medizin-Eur. J. Ultrasound*, vol. 34, pp. 169–184, Apr. 2013.

[11] J.-L. Gennisson, T. Deffieux, M. Fink, and M. Tanter, "Ultrasound elastography: Principles and techniques," *Diagnostics Intervent. Imag.*, vol. 94, pp. 487–495, May 2013.

[12] L. Yuan and P. C. Pedersen, "Analytical phase-tracking-based strain estimation for ultrasound elasticity," *IEEE Trans. Ultrason., Ferroelectr., Freq. Control*, vol. 62, no. 1, pp. 185–207, Jan. 2015.

[13] R. Zahiri-Azar and S. E. Salcudean, "Motion estimation in ultrasound images using time domain cross correlation with prior estimates," *IEEE Trans. Biomed. Eng.*, vol. 53, no. 10, pp. 1990–2000, Oct. 2006.

[14] A. Dibattista and J. Noble, "An efficient block matching and spectral shift estimation algorithm with applications to ultrasound elastography," *IEEE Trans. Ultrason., Ferroelect., Freq. Control*, vol. 61, no. 3, pp. 407–419, Mar. 2014.

[15] M. G. Kibria and M. K. Hasan, "A class of kernel based real-time elastography algorithms," *Ultrasonic*, vol. 61, pp. 88–102, Aug. 2015.

[16] A. Ramalli, O. Basset, C. Cachard, E. Boni, and P. Tortoli, "Frequency-domain-based strain estimation and high-frame-rate imaging for quasi-static elastography," *IEEE Trans. Ultrason., Ferroelect., Freq. Control*, vol. 59, no. 4, pp. 817–824, Apr. 2012.

[17] J. Jiang and T. J. Hall, "A coupled subsample displacement estimation method for ultrasound-based strain elastography," *Phys. Med. Biol.*, vol. 60, no. 21, pp. 8347–8364, 2015.

[18] H. Rivaz, E. Boctor, M. A. Choti, G. D. Hager, "Ultrasound elastography using multiple images," *Med. Image Anal.*, vol. 18, no. 2, pp. 314–329, 2014.

[19] H. Rivaz, E. Boctor, P. Foroughi, R. Zellars, G. Fichtinger, and G. Hager, "Ultrasound elastography: A dynamic programming approach," *IEEE Trans. Med. Imag.*, vol. 27, no. 10, pp. 1373–1377, Oct. 2008.

[20] J. Jiang and T. J. Hall, "A regularized real-time motion tracking algorithm using dynamic programming for ultrasonic strain imaging," in *Proc. IEEE Ultrason. Symp.*, Vancouver, BC, Canada, Oct. 2006, pp. 606–609.

[21] C. Pellot-Barakat, F. Frouin, M. F. Insana, and A. Herment, "Ultrasound elastography based on multiscale estimations of regularized displacement fields," *IEEE Trans. Med. Imag.*, vol. 23, no. 2, pp. 153–163, Feb. 2004.

[22] S. K. Alam, J. Ophir, and E. E. Konofagou, "An adaptive strain estimator for elastography," *IEEE Trans. Ultrason., Ferroelect., Freq. Control*, vol. 45, no. 2, pp. 461–472, Mar. 1998.

[23] X. Pan, J. Gao, S. Tao, K. Liu, J. Bai, and J. Luo, "A two-step optical flow method for strain estimation in elastography: Simulation and phantom study," *Ultrasonics*, vol. 54, no. 4, pp. 990–996, Apr. 2014.

[24] X. Pan *et al.*, "Performance comparison of rigid and affine models for motion estimation using ultrasound radio-frequency signals," *IEEE Trans. Ultrason., Ferroelect., Freq. Control*, vol. 62, no. 11, pp. 1928–1943, Nov. 2015.

[25] M. A. Hussain, E. M. Abu Anas, S. K. Alam, S. Y. Lee, and M. K. Hasan, "Direct and gradient-based average strain estimation by using weighted nearest neighbor cross-correlation peaks," *IEEE Trans. Ultrason., Ferroelect., Freq. Control*, vol. 59, no. 8, pp. 1713–1728, Aug. 2012.

[26] M. A. Hussain, F. Alam, S. A. Rupa, R. Awwal, S. Y. Lee, and M. K. Hasan, "Lesion edge preserved direct average strain estimation for ultrasound elasticity imaging," *Ultrasonics*, vol. 54, pp. 137–146, Jan. 2014.

[27] T. Varghese, E. E. Konofagou, J. Ophir, S. K. Alam, and M. Bilgen, "Direct strain estimation in elastography using spectral cross-correlation," *Ultrasound Med. Biol.*, vol. 26, pp. 1525–1537, Nov. 2000.

[28] E. E. Konofagou, T. Varghese, J. Ophir, and S. K. Alam, "Power spectral strain estimators in elastography," *Ultrasound Med. Biol.*, vol. 25, pp. 1115–1129, Sep. 1999.

[29] S. K. Alam, F. L. Lizzi, T. Varghese, E. J. Feleppa, and S. Ramachandran, "Adaptive spectral strain estimators for elastography," *Ultrasonic Imag.*, vol. 26, pp. 131–149, Jul. 2004.

[30] A. Nahiyan and M. K. Hasan, "Hybrid algorithm for elastography to visualize both solid and fluid-filled lesions," *Ultrasound Med. Biol.*, vol. 41, pp. 1058–1078, Apr. 2015.

[31] M. K. Hasan, E. M. A. Anas, S. K. Alam, and S. Y. Lee, "Direct mean strain estimation for elastography using nearest-neighbor weighted least-squares approach in the frequency domain," *Ultrasound Med. Biol.*, vol. 38, pp. 1759–1777, Oct. 2012.

[32] U. Bae and Y. Kim, "Direct phase-based strain estimator for ultrasound tissue elasticity imaging," in *Proc. 26th Annu. Int. Conf. IEEE Eng. Med. Biol. Soc.*, vol. 1. Sep. 2004, pp. 1345–1348.

[33] S. R. Ara *et al.*, "Phase-based direct average strain estimation for elastography," *IEEE Trans. Ultrason., Ferroelect., Freq. Control*, vol. 60, no. 11, pp. 2266–2283, Nov. 2013.

[34] G. F. Pinton, J. J. Dahl, and G. E. Trahey, "Rapid tracking of small displacements with ultrasound," *IEEE Trans. Ultrason., Ferroelect., Freq. Control*, vol. 53, no. 6, pp. 1103–1117, Jun. 2006.

[35] H. Rivaz and D. L. Collins, "Near real-time robust non-rigid registration of volumetric ultrasound images for neurosurgery," *Ultrasound Med. Biol.*, vol. 41, pp. 574–587, Feb. 2015.

[36] G. D. Hager and P. N. Belhumeur, "Efficient region tracking with parametric models of geometry and illumination," *IEEE Trans. Pattern Anal. Mach. Intell.*, vol. 20, no. 10, pp. 1025–1039, Oct. 1998.

[37] S. Baker and I. Matthews, "Lucas-Kanade 20 years on: A unifying framework," *Int. J. Comput. Vis.*, vol. 56, no. 3, pp. 221–255, 2004.

[38] E. K. P. Chong and S. H. Zak, *An Introduction to Optimization*, 3rd ed. New York, NY, USA: Wiley, 2008.

[39] S. J. Wright and J. Nocedal, *Numerical Optimization*. New York, NY, USA: Springer-Verlag, 1999.

[40] X. Pan, K. Liu, J. Bai, and J. W. Luo, "A regularization-free elasticity reconstruction method for ultrasound elastography with freehand scan," *Biomed. Eng. Online*, vol. 13, no. 1, p. 132, Sep. 2014.

[41] T. Varghese and J. Ophir, "An analysis of elastographic contrast-to-noise ratio," *Ultrasound Med. Biol.*, vol. 24, no. 6, pp. 915–924, 1998.

[42] J. A. Jensen, "Field: A program for simulating ultrasound systems," *Med. Biol. Eng. Comput.*, vol. 34, no. 1, pp. 351–353, 1996.

[43] T. Krouskop, T. Wheeler, F. Kallel, B. Garra, and T. Hall, "The elastic moduli of breast and prostate tissues under compression," *Ultrasound Imag.*, vol. 20, pp. 260–274, Nov. 1998.

[44] J. Liu, C. K. Abbey, and M. F. Insana, "Linear approach to axial resolution in elasticity imaging," *IEEE Trans. Ultrason., Ferroelect., Freq. Control*, vol. 51, no. 6, pp. 716–725, Jun. 2004.

[45] R. Padgett and C. J. Kotre, "Assessment of the effects of pixel loss on image quality in direct digital radiography," *Phys. Med. Biol.*, vol. 49, p. 977, Mar. 2004.

[46] M. M. Doyley, Q. Feng, J. B. Weaver, and K. D. Paulsen, "Performance analysis of steady-state harmonic elastography," *Phys. Med. Biol.*, vol. 52, pp. 2657–2674, May 2007.

[47] E. K. Abdalla *et al.*, "Recurrence and outcomes following hepatic resection, radiofrequency ablation, and combined resection/ablation for colorectal liver metastases," *Ann. Surgery*, vol. 239, pp. 818–827, Jun. 2004.